Exp Fluids (2013) 54:1598
DOI 10.1007/s00348-013-1598-z

RESEARCH ARTICLE

Experiments on transitional shock wave–boundary layer interactions at Mach 5

E. Erdem · K. Kontis · E. Johnstone · N. P. Murray · J. Steelant

Received: 27 March 2013 / Revised: 31 July 2013 / Accepted: 2 September 2013 / Published online: 28 September 2013
© Springer-Verlag Berlin Heidelberg 2013

Abstract An experimental campaign was carried out to investigate transitional shock wave–boundary layer interactions (SWBLI) at Mach and unit Reynolds numbers of 5 and 15.9×10^6 1/m, respectively. An impinging shock that generates 7° flow deflection resulted in separated SWBLI flowfield on axisymmetric centrebody. Various flow diagnostics were utilised such as schlieren photography, quantitative infrared thermography, shear sensitive liquid crystals, pressure sensitive paints and particle image velocimetry (PIV) to provide a complete time-averaged experimental data set. One nominally laminar case (with triggered transition due to SWBLI) and four natural transition cases with varying intermittency were tested. Heat transfer and shear stress peaks occurred around the reattachment point. For nominally laminar case, the separation induces transition, and thus, heat transfer and pressure peaks were found to be the highest. For the cases with natural transition with different intermittency levels, where incoming boundary layer is in state of transition, the magnitude of pressure and heat transfer peaks initially started to increase reaching a maximum and afterwards decreased towards the highest intermittency case. The presence of streamwise vortices was apparent for laminar case. Pressure peaks were found to occur slightly downstream of heat flux/shear stress peaks. PIV results (for laminar case only) showed high levels of turbulence above the separation region, proving triggered transition behaviour.

E. Erdem · K. Kontis (✉)
AeroPhysics Laboratory, School of Engineering, University of Glasgow, Glasgow G12 8QQ, UK
e-mail: kostas.kontis@glasgow.ac.uk

E. Erdem
e-mail: erincerdem@gmail.com

E. Johnstone
Fluid Gravity Engineering, The Old Coach House, 1 West Street, Emsworth 10 7DX, UK
e-mail: emma.johnstone@fluidgravity.co.uk

N. P. Murray · J. Steelant
European Space Research and Technology Centre, Postbus 299, Keplerlaan 1, 2200 AG Noordwijk, The Netherlands
e-mail: neil.paul.murray@esa.int

J. Steelant
e-mail: johan.steelant@esa.int

1 Introduction

Flow past a hypersonic vehicle is the seat of strong shock waves forming at vehicle nose, rounded leading edge of wings and tails, air intake compression ramps of an air-breathing propulsion system, control surfaces, rear part of an afterbody where the nozzle jets meet the outer stream, to name the most salient examples (Arnal and Delery 2004). When these shock waves interact with boundary layers developing on solid surfaces shock wave–boundary layer interactions (SWBLIs) form, which embed a series of complicated flow phenomena such as flow separations, shear layers, transition mechanisms and shock–shock interactions. SWBLI can induce separation which causes loss of a control surface effectiveness and drop of an air intake efficiency, and it may be the origin of large-scale fluctuations such as air intake buzz, buffeting or fluctuating side loads in separated propulsive nozzles. The subsequent reattachment of the separated shear layer on a nearby surface gives rise to local heat transfer rates, which can be far in excess of those of an attached boundary layer (Edney 1968). Because of their dramatic importance, SWBLIs have been extensively studied during the past 50 years and

are still the subject of active research due to their complexity and difficulty to predict their behaviour, especially in transitional/turbulent regime (Delery and Marvin 1986; Holden 1986; Settles 1993). The large amount of experimental results on SWBLI in 2-D flows allowed a clear identification of the role played by the main parameters involved in the interaction process. Also correlation laws have been deduced for numerical validation, giving the upstream interaction length, the limit for shock induced separation and, of prime importance in hypersonic flows, the peak heat transfer at reattachment.

During the ascent or descent of a space vehicle, it encounters a wide range of Reynolds numbers which results in boundary layer flows covering the complete vehicle either in a fully laminar, turbulent or transitional state. Most of the SWBLI work done over the years has been focussed on fully developed turbulent flows since most practical applications were at transonic and low supersonic speeds at altitudes where Reynolds numbers are large and turbulent boundary layer flows are encountered. Whereas laminar SWBLIs are likely to occur at high altitudes, the rise in Reynolds number during the descent shifts the transition point from the rear towards the front and hence can cross the SWBLI region. Therefore, transitional SWBLIs, in which the incoming boundary layer is in a transitional state (natural transition), or in which transition is induced within the interaction itself (triggered transition), appear to be even more unsteady and could have greater adverse effects, and yet have received little attention (Vandomme et al. 2006). If transition occurs not far from a SWBLI region, the interaction can lead to intense heat fluxes higher than those observed in turbulent interactions (Bur and Chanetz 2009). As a matter of fact for most of the measured/simulated laminar SWBLI cases, the boundary layer undergoes triggered transition due to the extreme sensitivity of the separated shear layer to disturbances. This transition mechanism produces a mixed interaction in which separation has the features of a laminar flow (decrease in the heat transfer), whereas reattachment has a turbulent behaviour (higher pressure and heat transfer peaks).

Two common interactions encountered between a shock wave and a boundary layer are the ramp flow and the impinging shock wave cases. The first case corresponds to a control surface or an air intake compression ramp, while the second case refers to shock reflection inside of an air intake of the mixed supersonic compression type (Arnal and Delery 2004). The former case has been extensively studied for a wide variety of flow conditions and configurations (Settles and Dodson 1991). The salient features of this type of interaction can be found in references given by Dolling (2001). For the latter case, a planar oblique shock impinges on a wall, and if the impinging shock is of sufficient strength, it can cause boundary layer separation. The resulting flow pattern comprised of separation region and separation shock, shock–shock interaction, expansion waves situated on top the SWBLI region, reattachment shock, unsteady shear layer, etc. This configuration has received less attention over the years. Supersonic impinging shock wave case with turbulent boundary layer was investigated in detail by Humble et al. (2007, 2009) examining the cause of unsteadiness of the interaction. On the other hand for hypersonic SWBLIs, only a few studies are available such as the ones from Schuelein et al. (1996), Knight et al. (2003), Boyce and Hillier (2000) and Murray et al. (2013). The studies from Boyce and Hillier (2000) and Murray et al. (2013) involved axisymmetric SWBLI configurations, avoiding three dimensional side effects. The test model used was a hollow axisymmetric centrebody on which natural transition took place, and the impinging shock was localised on turbulent boundary layer. Obtained pressure and heat transfer distributions assessed the severity of the interaction in terms of the associated peaks, and oil flow visualisation demonstrated Goertler type vortices at the reattachment.

In terms of transitional hypersonic SWBLIs, there is a clear need for detailed experimental investigations, which can provide a better insight into the interaction behaviour and can serve as a basis for thorough numerical validation and also for deducing empirical correlations. For modelling and simulation purposes, a database build-up is crucial in particular for transitional flow. In the past, European Space Agency (ESA) has launched a similar activity for purely turbulent flow both with experimental (Schuelein et al. 1996) and modelling initiatives (Steelant and Dick 2001; Steelant 2002). Present experimental study focusses on this problem with an impinging shock wave including both transition mechanisms: natural and triggered transition. The methodology involves high-speed wind tunnel testing at Mach 5 with an axisymmetric hollow model similar to studies of Boyce and Hillier (2000) and Murray et al. (2013). The associated flow diagnostics include conventional stagnation and wall pressure measurements, schlieren visualisation, quantitative infrared thermography (QIRT), shear sensitive liquid crystals (LC), pressure sensitive paints (PSP) and particle image velocimetry (PIV). The objective of this study is to provide a complete time-averaged experimental data set for transitional hypersonic SWBLI due to an impinging shock wave, which is not available in the literature. The effect of intermittency on SWBLI is also studied.

2 Experimental methodology

2.1 Experimental facility

The experiments documented herein were performed in high supersonic tunnel (HSST) in Aero-Physics Laboratory

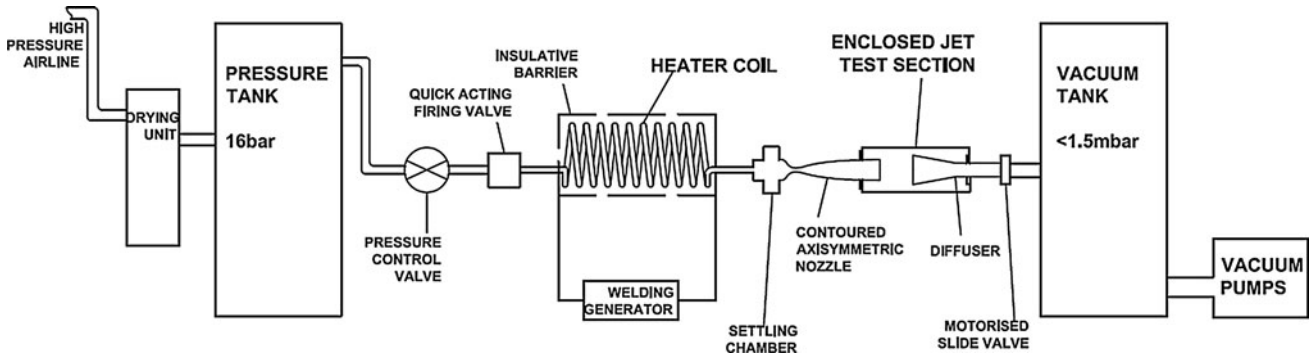

Fig. 1 University of Manchester HSST schematic layout

of the University of Manchester. The tunnel is of the intermediate blowdown (pressure–vacuum) type which uses dry air as the working fluid and is shown schematically in Fig. 1. The various components of this facility have been discussed in detail elsewhere (Erdem and Kontis 2010; Erdem et al. 2012a), and hence, a summary of the important features is included. Air from a high pressure airline is dried and stored in a pressure vessel at a pressure over 15 bar. After passing through a pneumatically operated quick acting ball valve, the gas enters the electric resistive heater section. The gas temperature is raised from ambient to a temperature between that sufficient to avoid liquefaction on its expansion through the nozzle and that of a maximum enthalpy flow condition of 700 K. On leaving the heater, air enters the settling chamber which is downstream of the flow straightener matrix. Immediately, downstream of the settling chamber is situated at contoured axisymmetric Mach 5 nozzle. The stagnation pressure can range from 5 to 8 bar, and thereby, unit Reynolds numbers, *Re/m*, of between 4 and 16 $\times$ 10^6 1/m can be achieved. The tunnel working section is an enclosed free jet design. The variations in Mach number and unit Reynolds number were found to be $\pm$0.4 and $\pm$3.7 %, respectively (Erdem and Kontis 2010; Erdem et al. 2012a). The useful running time is found to be 7.5 s. The incoming turbulence intensity of HSST is found to be <1 % in the core flow, which is measured by two component PIV using ensemble averaging of 200 vector fields.

2.2 Models

For QIRT measurements, a model made of a low conductivity material is needed so that heat transferred from Mach 5 flow to the surface would not penetrate inside the material quickly. This allows the use of semi-infinite 1-D unsteady heat conduction assumption to deduce heat flux from the wall temperature history. Thus, a hollow centrebody model, made of PEEK, is used for the experimental campaign. The model is 50.8 mm in diameter and 450 mm

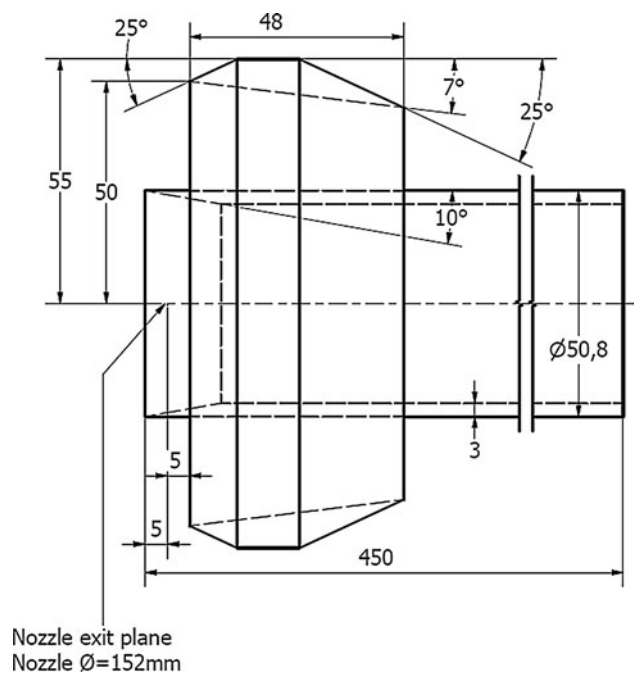

Fig. 2 Technical drawing of cowl and its starting position (SWBLI@90 mm) with respect to the centrebody

in length with a wall thickness of 3 mm as shown in Fig. 2 and is painted with matt black paint to increase emissivity. Due to the brittle nature of model material, nonuniformities are present at the sharp leading edge, which are characterised by a mechanical measurement device (see Sect. 2.3.7). The centrebody is placed inside an axisymmetric hollow brass section that is connected to an A-support. This support mechanism is situated on a brass plate that can move back and forth. In terms of the shock generator to create SWBLI, an axisymmetric cowl model, made of aluminium, is manufactured. The flow deflection introduced by the cowl is 7° from inside as shown in Fig. 2. The cowl design was based on various factors in mind such as desired impinging shock strength, optical access, tunnel unstart and clean SWBLI region (free of cowl expansion fan and nozzle shock interference). The cowl is placed on

an I-section stand that is fixed on another brass plate as shown in Fig. 3. The relative orientation of the centrebody with respect to the cowl is checked using a telescopic gauge that measures the distance between two concentric bodies at quadrants. The misalignment in vertical and lateral directions is found to be <0.3°. Same apparatus is used to make sure that the orientation of centrebody with respect to Mach 5 nozzle is within small limits.

2.3 Flow diagnostics

2.3.1 Pressure and temperature measurements

Stagnation and wall static pressure measurements are done using high-sensitivity Kulite© pressure transducers. A pitot probe (3 mm in diameter) attached to a Kulite pressure transducer (XTE-190M, 100 psi range) via small chamber and a K-type thermocouple probe (3 mm in diameter) with a junction diameter of 1.0 mm are located at the settling chamber to measure stagnation pressure, p_0 and stagnation temperature, T_0 respectively. In case of wall pressure measurements, 12 pressure tappings (of 1.5 mm outer diameter) are located on the model; the first three tappings are offset by 20° with respect to the centreline, whereas the others are located at the centreline as shown in Table 1. These pressure tappings are connected to hyperdermic metal tubings that are running through inside of the centrebody, and they are attached to the flexible heat resistant tubings. Then, these flexible tubings are connected to Kulite pressure transducers (XTE-190M, 0.7 bar range) via transducer block. The linearity of transducers is maintained by vacuum calibration using pressure and Pirani gauges situated in the test section ceiling.

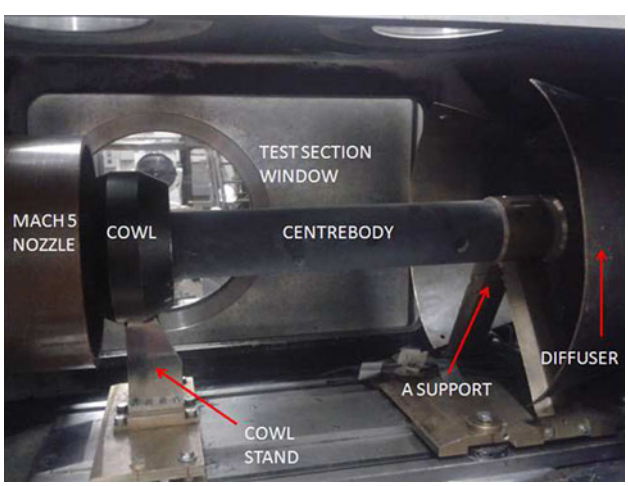

Fig. 3 Test section of HSST with the centrebody and cowl

Table 1 Locations of pressure tappings for PEEK centrebody

Tapping no.	Location from leading edge (mm)	Azimuthal angle (°)
1	70	−20
2	90	−20
3	110	−20
4	170	0
5	180	0
6	190	0
7	200	0
8	210	0
9	220	0
10	240	0
11	255	0
12	270	0

Analogue signals from all the sensors are acquired at 5 kHz by a high-speed data acquisition (DAQ) card, National Instruments (NI)© PCI-6251, after they are conditioned by SXCI-1000 unit. This signal conditioning unit enables various modules to be inserted for different applications and provide hardware filtering. Current modules are SCXI-1520 compatible with pressure or load measurements and SCXI-1112 for temperature measurements. The existing system had the capability of collecting data at a frequency up to 333 k samples/s at 16 bit digitisation. The DAQ has a fully programmable environment; it can generate digital or analogue signals at a precise time by means of software, LABVIEW v.8.5 (Erdem and Kontis 2010; Erdem et al. 2012a).

2.3.2 Schlieren photography

Toepler's z-type Schlieren technique is adapted for flow visualisation that consist of a continuous light source of Palflash 501 (pulse photonics) with a focusing lens and a 1 mm wide slit, two 203.2 mm inches parabolic mirrors with 1,828.8 mm focal length, a knife edge, a set of Hoya 49 mm close-up lenses and a digital Canon SLR camera, EOS-450D, 12MP. The offset angle of parabolic mirrors with respect to their axis is set to 5° to prevent optical aberrations such as coma and astigmatism as much as possible (Erdem and Kontis 2010; Erdem et al. 2012a). Parallel beam of light is passed through test section windows before focusing on the knife edge plane that is placed perpendicular to flow direction, and the focused beam is shone on CMOS sensor of the camera. The camera is set to have a long shutter, and the light source is set to spark mode (pulse duration 0.75 μs to resolve flow features with sharpness). The layout of the optical setup and the DAQ

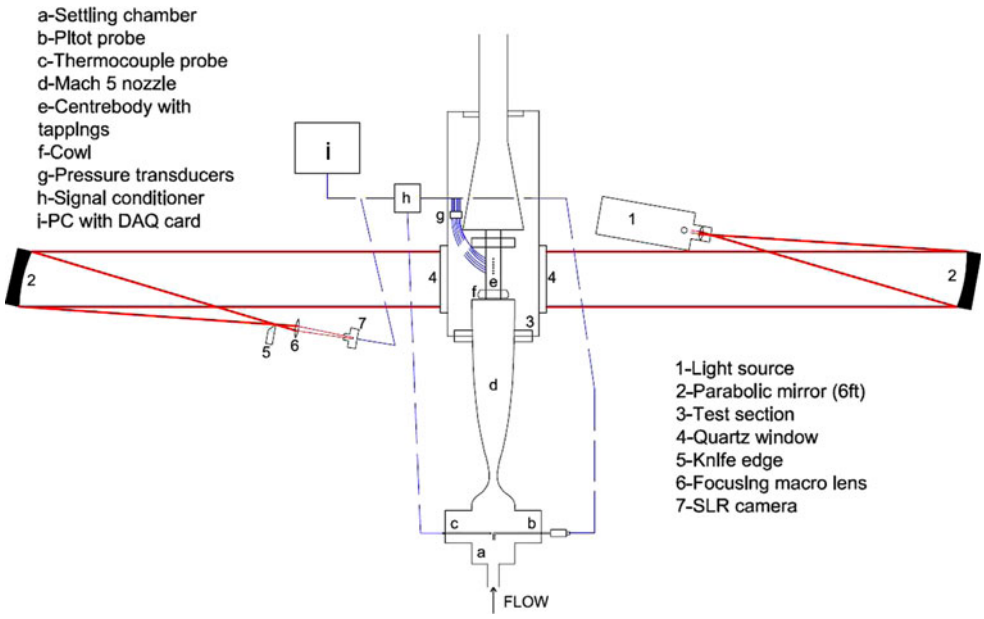

Fig. 4 Schematic setup of schlieren visualisation with DAQ architecture (Erdem and Kontis 2010; Erdem et al. 2012a)

architecture with measurement chain for conventional pressure and temperature measurements is shown in Fig. 4.

2.3.3 *Quantitative infrared thermography (QIRT)*

The change of surface temperature distribution is measured using infrared camera (FLIR SC655), which has a temperature range of −20 to 150 °C with accuracy of ±1 %. The spectral range of the camera is between 7.5 and 13 μm. It is installed on the top of the test section and views the model obliquely at 25° with respect to vertical through a Germanium window with transmission range of 3–12 μm. The model is painted matt black (see Sect. 2.2) to increase the surface emissivity, which is estimated to be 0.95. The transmission ratio of the Germanium window and the test gas is assumed to be 0.97. The surface temperature is recorded in the entire test duration at 100 Hz at 640 × 240 pixel^2 resolution. Figure 5 shows the setup for QIRT measurements.

2.3.4 *Shear-sensitive liquid crystals (LC)*

The shear sensitive liquid crystal mixture is mixed with acetone to form a solution and applied on matt black centrebody surface with a spray gun. After its application inside the test section, the centrebody is left to dry and the mixture takes rusty red colour on the surface, and during the test, it changes colour based on the wall shear stress level that changes the crystalline structure of the mixture. A Canon SLR camera, EOS-600D, 18 MP and an 800 W light source are placed over the test section in "*V*" type configuration. The camera is run at 6 fps at full resolution, and the exposure is 8 ms. Figure 6 shows the setup for LC measurements, which is similar to Kontis and Stollery (1999).

2.3.5 *Pressure sensitive paints (PSP)*

The pressure sensitive paint is composed of Ruthenium, Ethanol, MTEOS and HCl and sprayed on top of the white base coat applied on the centrebody. This PSP is a polymer-based paint and has superior pressure sensitivity; however, it has a slower response time compared to porous PSP as reported by Quinn et al. (2011). In a polymer PSP, the luminophore is embedded in a polymer layer, which is the binding material. With the excitation of the paint by an appropriate light source, luminophores become excited and emit luminescence. This phenomenon is quenched by the presence of the oxygen and temperature. For the excitation of PSP, a pair of light emitting diode (LED) panels with a peak wavelength, $\lambda > 470$ nm is used. Each LED panel is comprised of 13 × 10 LED arrays. The LED panel is placed on each side of test section. The main advantage of placing two LED panels, as shown in Fig. 7, on both sides of test section is that it can provide a uniform illumination on the surface of model. The centrebody is rotated 90° to have the same area as in QIRT/LC tests assuming the cowl is perfectly axisymmetric. A 12 bit LaVision Image Intense CCD camera with 1,280 × 1,040 pixel^2 resolution is used for emission acquisition at 9 fps with 10 ms exposure time. The camera covers the spectral range from 290 to 1,100 nm, but has its maximum quantum efficiency about 65 % at 500 nm. The lowest emission signal is found to be 921 counts (22.5 % of the full 12-bit camera chip

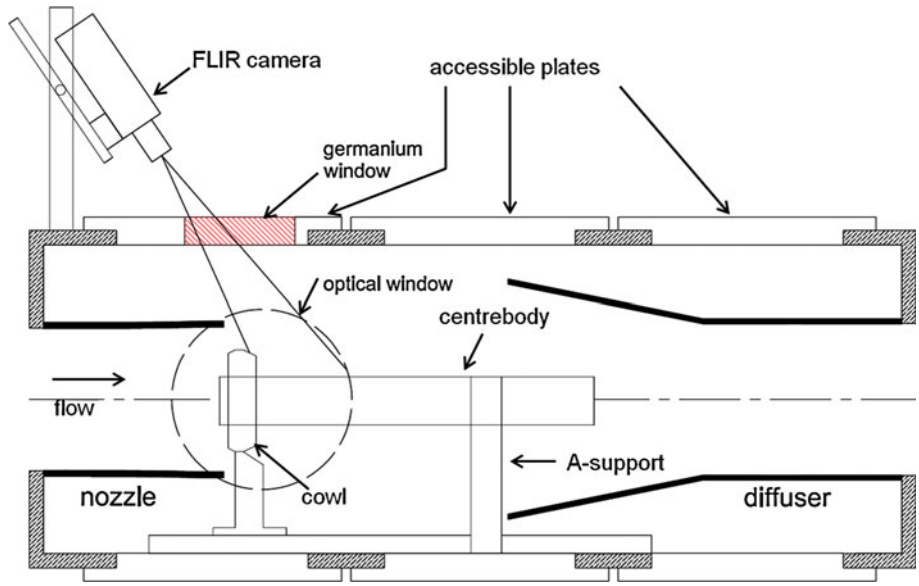

Fig. 5 Schematic setup of QIRT measurements

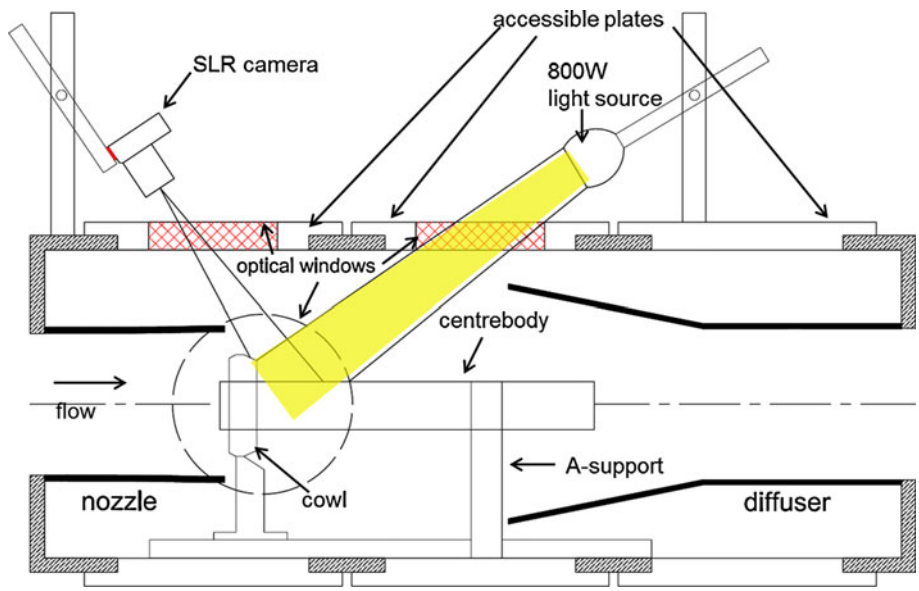

Fig. 6 Schematic setup of LC measurements

capacity) for PSP tests, which satisfies measurement requirements. The wavelength emitted from platinum-based pressure sensitive paint is found to be around 610 nm using a spectrometer. Different wavelength filters are required to separate the emission from the illumination. Based on the spectral analysis, a combination of orange 550-nm-long-pass and an IR rejection filter is employed in front of the CCD camera. The former allows the transmission of light with $\lambda > 550$ nm while the latter rejects light with wavelength longer than 700 nm. The camera is connected to a computer for image acquisition and operated by Davis 7.2 software. The procedure and the setup are similar to studies of Yang et al. (2011, 2012a, b)

2.3.6 Particle image velocimetry (PIV) measurements

Two component PIV measurements on the centreline of the centrebody are carried out with a dedicated PIV system, which includes a seeding device that discharge particles through an orifice, an illuminating laser with related optics to create a laser sheet and a recording camera. The following subsections describe the subsystems that were reported by Erdem et al. (2012b, c).

Aluminium oxide powder particles with a nominal crystal size of 300 nm are used with a nominal bulk density of $\rho_p = 3{,}970$ kg/m^3 for tests. PS-10 powder seeder device (see Fig. 8) is used to generate an airflow seeded with particles. This device consists of a rotating powder

containing drum that is controlled by an electronic motor inside a pressure vessel. The drum is rotated about a horizontal axis, and at each revolution of the drum, a small amount of powder is dispensed through a small opening. Inside the vessel are situated six sonic break-up jets to prevent agglomeration of the particles and baffles that are attached to outer perimeter of the drum also help to agitate heavy agglomerates. In order to prevent powder particles leaking back to the upstream half of the vessel and contaminating the region where the electric motor is housed, purge air is continuously supplied. Single exit port of 10 mm is located on the side of the chamber to allow seeded airstream flow towards the rig via an air tube. The air tube is connected to a seeding rake that is placed at the settling chamber of HSST.

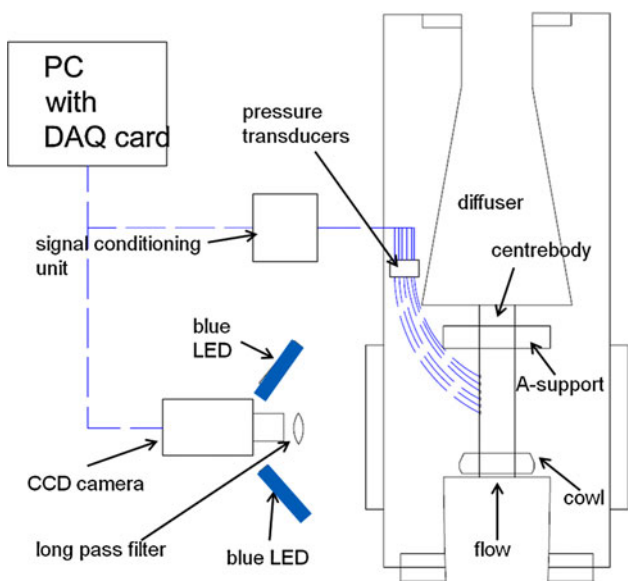

Fig. 7 Schematic setup of PSP measurements

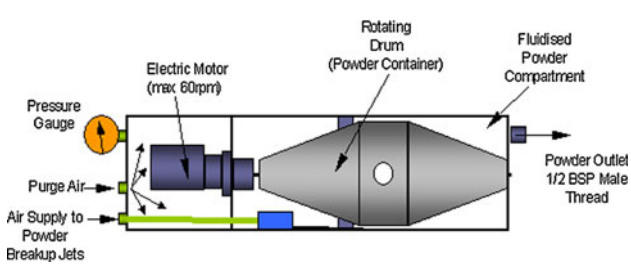

Fig. 8 Schematic of PS-10 powder seeder device

The flow tracing capability of particles of diameter d_p and a particle density ρ_p is usually quantified through the particle relaxation time, τ_p. The theoretical behaviour for small spherical particles may be reduced to the modified Stokes drag law defined by Melling (1997). Given the relatively low value of the Mach number and Reynolds number based on the particle diameter, the modified drag relation that takes into account rarefaction effects yields the expression for the relaxation time in Eq. 1, where Kn_d is the Knudsen number, which is defined in Eq. 2. Re_d is the Reynolds number based on the diameter of the particle, and M_v is the Mach number both evaluated for the maximum particle slip velocity, ΔV (Scarano 2008).

$$\tau_p = \frac{\rho_p d_p^2 (1 + 2.7 Kn_d)}{18\mu} \tag{1}$$

where

$$Kn_d = 1.26\sqrt{\gamma}(M_v/Re_d). \tag{2}$$

As suggested by Samimy and Lele (1991), the particle dynamic effects may be further parameterised by the Stokes number written in Eq. 3. For accurate flow tracking, the timescale of the flow has to be bigger than the time response of the particles, i.e. $Sk \ll 1$. The characteristic flow timescale is found as 25 µs by assuming ΔV as u_∞ (see Table 2) and δ as 2 mm (see Eq. 3), whereas the particle time response is calculated as 30 µs using typical freestream conditions ($T_0 = 370$ K, $p_0 = 7{,}950$ mbar, $u_\infty = 790$ m/s). Therefore, the Stokes number for the current tests is found to be around 1.2, indicating doubts about the particles tracking the flow with fidelity. The relaxation time for aluminium oxide powder particles was found to be <4 µs in ref. Erdem et al. (2012b) using ensemble averaging.

$$Sk = \frac{\tau_p}{\tau_f} \quad \text{where} \quad \tau_f = 10\frac{\delta}{\Delta V} \approx 10\frac{\delta}{u_\infty} \tag{3}$$

A Litron Nano L series, Nd:Yag Q-switched laser is used for PIV illumination. The laser has the pulse energy of 200 mJ at repetition rate of 15 Hz. The laser beams are pulsed at the wavelength of 532 nm. The pulse width of the light is 4 ns, and the pulse separation time (the time interval between two consecutive PIV images light pulses, Δt) can be adjusted up to 0.1 µs as minimum in conjunction with image recording. A laser sheet of 0.5 mm thickness is produced with a series of spherical and

Table 2 Experimental test conditions at Mach 5

M_∞ (%)	p_0 (mbar) (%)	T_0 (°K) (%)	Re/m (10^6 1/m) (%)	p_∞ (mbar) (%)	u_∞ (m/s) (%)	T_{wall} (initial) (°K) (%)
5 ± 0.2	7,968 ± 0.7	372.4 ± 1.7	15.9 ± 2.5	14.94 ± 1.3	790 ± 0.7	293 ± 1.0

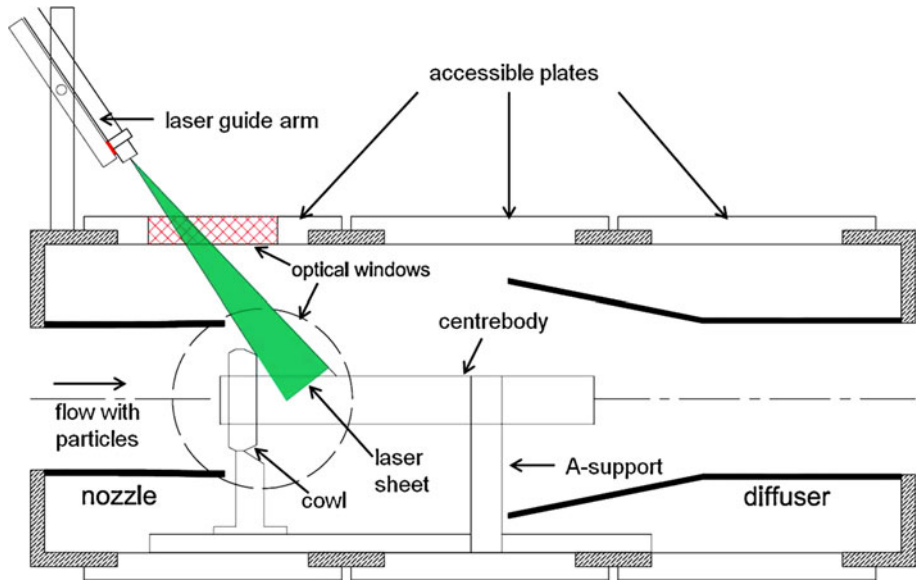

Fig. 9 Schematic setup of PIV measurements

cylindrical lenses and routed above the test section via laser guide arm. A LaVision Imager ProX2M CCD camera with 1,600 × 1,200 pixel^2 resolution is used to record scattered light reflecting from particles at 14 bit digitisation. The camera is equipped with a Nikon 60 mm focal objective lens with f number of 5.6, in combination with a narrow-bandpass 532 nm filter in order to minimise ambient light interference. The camera views the laser sheet orthogonally at a desired field of view (FoV) of 60 × 45 mm^2. Whole operation is synchronised and run using the DaVis 7.2 software with a programmable timing unit (PTU). Figure 9 shows the setup for PIV measurements.

2.3.7 *Leading edge measurements of PEEK model*

As the transition location is generally very sensitive to the leading edge nonuniformities, significant effort is taken to ensure the leading edge is uniform; however due to the brittle nature of PEEK material, there are some imperfections. These imperfections are characterised by a Mitutoyo Contracer CV-3100, which employs a needle tracking the surface. The tie wrap used provides a starting point for the needle. The needle with a tip radius of 25 μm, climbs over the centrebody and follows the contour as shown in Fig. 10. The leading edge thickness profiles for various angles around circumference ranging from −50° to 50° are also shown in Fig. 10. The plateau, shown in the profiles before origin, depicts the tip of the centrebody leading edge; the bigger the plateau the thicker the leading edge. The thickness is found to be <100 μm for most of the azimuthal locations; however, the section of the centrebody with negative azimuthal angles is found to be blunter compared to positive side. For small bluntness, transition onset is found to be delayed (Simeonides 2003), and hence, for the same unit Reynolds number and running length upstream of the transition onset, skin friction and heat transfer would be smaller for a blunter model.

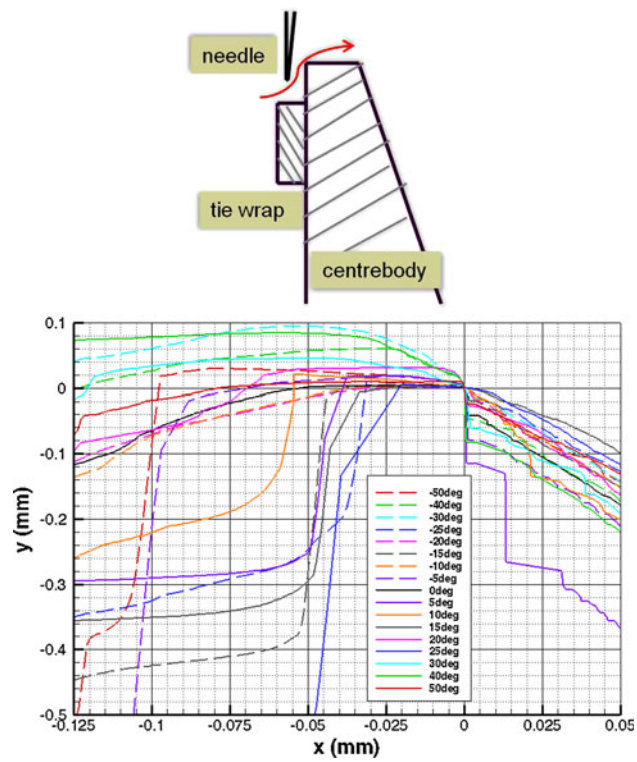

Fig. 10 *Top* leading edge thickness measurements with Mitutoyo Contracer CV-3100; *bottom* leading edge thickness profiles at various locations around the centrebody

3 Results

The results of the experimental campaign include schlieren photography, QIRT, LC, PSP and wall pressure measurements, and PIV measurements.

3.1 Upstream conditions and intermittency regions

The upstream conditions are deduced from p_0 and T_0 signals, and p_0 signals are shown in Fig. 11 with the time-averaging window. p_0 signals only from QIRT tests are shown here for brevity including the tests without the presence of the cowl. Due to the high supply pressure to achieve maximum unit Reynolds number, the stagnation pressure exhibits a gradual drop during the useful running time; nevertheless, the time-averaging window is chosen where p_0 signal varies <1 % over a second from 0.6 to 1.6 s. Useful flow time is reached 0.6 s after the flow starts. Table 2 summarises the upstream conditions deduced from all the tests. The uncertainties in experimental values are calculated using the approach from Moffat (1988).

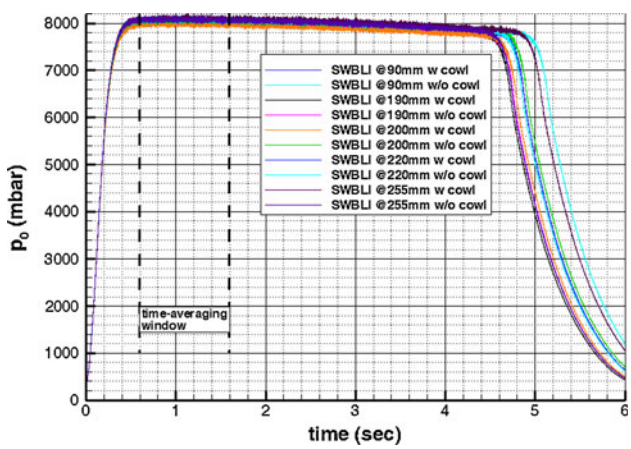

Fig. 11 Upstream flow conditions for QIRT tests

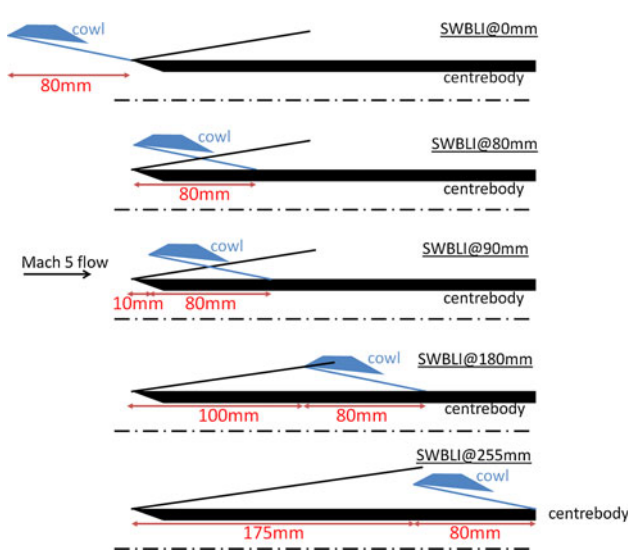

Fig. 12 The range of SWBLI locations

To theoretically estimate the transition location on the centrebody, an approach by Simeonides (2003) is employed. In this approach, flat plate transition data from several different facilities were collected, and a unique way was proposed to correlate this data with characteristic parameters such as leading edge thickness and viscous interaction parameter. Transition phenomenon was then classified into two major categories: viscous-dominated transition and bluntness-dominated transition. The parameter defining this classification is simply the ratio of a bluntness parameter, $\beta = M^2/(x/b)^{2/3}$, to viscous interaction parameter, $\bar{\chi} = M^3\sqrt{C/Rex_{tr}}$ at the transition location. C is the Chapman–Rubesin constant, which is the ratio of the density multiplied by viscosity, μ at the wall to the freestream. If $\beta/\bar{\chi}$ is >1.9, then the transition is bluntness-dominated transition, otherwise it is viscous-dominated transition. When data are separated, two very good correlation plots can be drawn, Re_{tr} against $Re/m/M$ for viscous-dominated transition and Mx_{tr}/b against Re_b/M^2 for bluntness-dominated transition, where x_{tr} is the streamwise location of transition and b is leading edge thickness.

Table 3 Experimental test matrix

Test no.	Measurement technique	SWBLI posn (mm)	p_0 (mbar)	T_0 (°K)
1	Schlieren	90	7,966	370.9
2	Schlieren	190	7,940	371.4
3	Schlieren	200	7,978	372.2
4	Schlieren	220	7,975	371.4
5	Schlieren	255	7,949	371.9
6	QIRT	90	7,916	367.6
7	QIRT	190	8,031	376.1
8	QIRT	200	8,008	377.1
9	QIRT	220	8,090	382.6
10	QIRT	255	8,105	383.6
11	LC	90	7,956	368.9
12	LC	190	7,948	371.0
13	LC	200	7,968	369.2
14	LC	220	7,925	372.1
15	LC	255	7,929	373.9
16	PSP + Kulite	90	7,890	372.5
17	PSP + Kulite	190	7,932	368.4
18	PSP + Kulite	200	7,964	367.4
19	PSP + Kulite	220	7,954	369.6
20	PSP + Kulite	255	7,979	371.4
21	PIV	90	7,979	369.8

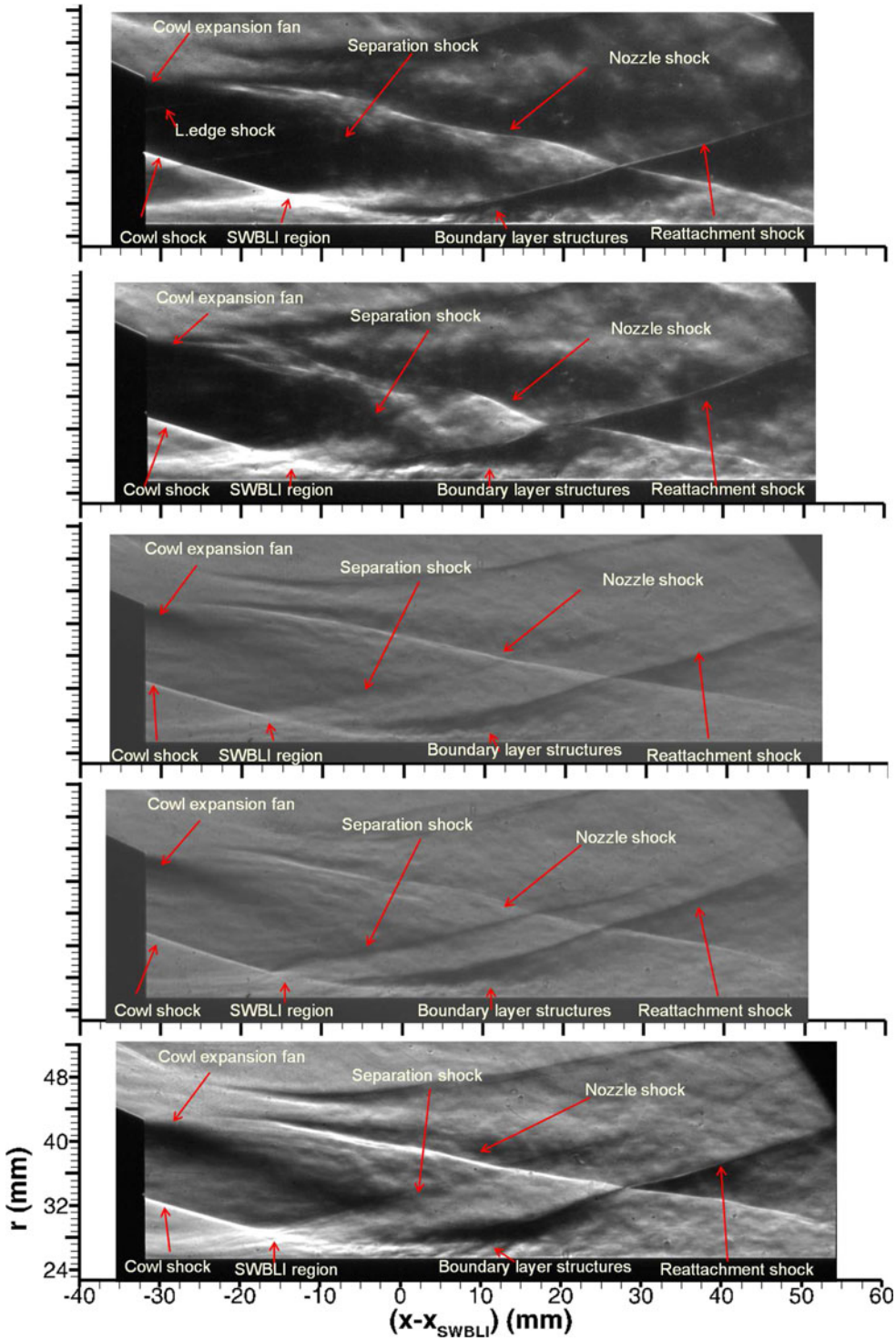

Fig. 13 Schlieren visualisation of the flowfield at the interaction region for SWBLI@90, 190, 200, 220 and SWBLI@255 mm cases in descending order

Therefore, x_{tr} is estimated as 140 mm from the bluntness-dominated transition plot for the highest attainable unit Reynolds number at Mach 5 (i.e. 16×10^6 1/m) and a leading edge thickness of 100 μm (see Sect.2.3.7).

The natural transition band on the centrebody is measured with QIRT without the cowl, and the band is found to cover a wide range of 150–300 mm (see Sect. 3.3). Then, SWBLI locations are determined using following criteria:

- A nominally laminar interaction (triggered transition), i.e. SWBLI to occur well before 150 mm but not close to the leading edge either

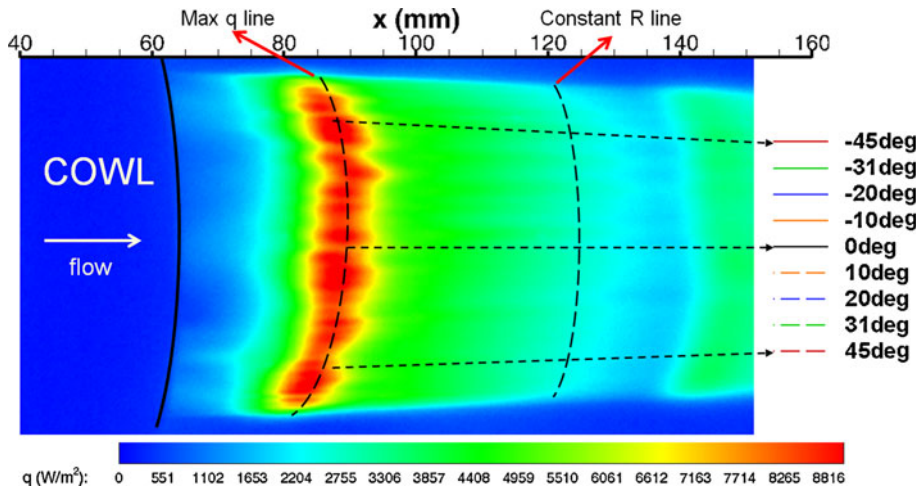

Fig. 14 Azimuthal heat flux data extraction showing constant R and maximum heat flux lines on the centrebody for SWBLI@90 mm case

- Centrebody leading edge shock should not interact with the cowl leading edge, i.e. SWBLI to occur after 180 mm
- Four transitional SWBLI configurations (natural transition) with different intermittencies

The approximated values of intermittency are found from QIRT tests for each case in Sect. 3.3. The range of SWBLI locations is shown in Fig. 12 with the inviscid position of the impinging shock and centrebody leading edge shock. The cowl is situated stationary 5 mm from the nozzle exit, and the centrebody is placed 10 mm ahead of cowl as shown in Fig. 2. This initial condition provides inviscid location of the impinging shock (inviscid SWBLI position) at 90 mm from the leading edge of the centrebody (i.e. SWBLI@90 mm nominally laminar case). Then, the intermittent cases of SWBLI@190, 200, 220 and 255 mm are achieved by moving the centrebody upstream by 100, 110, 130 and 165 mm, respectively, in addition to the original offset of 10 mm. The test matrix showing the cases tested with associated flow diagnostics is shown in Table 3.

3.2 Schlieren visualisation

Figure 13 shows spark schlieren visualisation of the flowfield with different SWBLI positions during the time-averaging window specified above. The horizontal axis is shifted with respect to SWBLI location, i.e. SWBLI location becomes zero ($x - x_{\mathrm{SWBLI}}$). Following structures can be observed clearly: centrebody leading edge shock (only visualised in SWBLI@90 mm case), impinging cowl shock, cowl expansion fan and the shear layer at the cowl trailing edge, upstream separation region (upstream of the shock impingement location) with the separation shock, expansion wave on top of the separation region, the reattachment shock and finally the nozzle shock. In the downstream of the SWBLI region, the boundary layer structures are oscillatory and turbulent in nature. In general, as the intermittency is increased, boundary layer becomes more turbulent and skin friction coefficient rises. Hence, it becomes more resistant to adverse pressure gradient imposed by the impinging shock, which would result in a relatively smaller SWBLI region. Nevertheless, due to blockage in optical access owing to cowl, the upstream extent of SWBLI region cannot be shown.

3.3 QIRT results

The data reduction for inferred heat flux distributions is as follows:

- From the full set of recordings including start-up and flow breakdown, windowing is done (10 images before flow starts and 200 images in total)
- Instantaneous temperature files are written in 2-D rectangular grid
- A numerical code is run using 1-D heat conduction equation to find instantaneous heat flux, q values using an approach from Cook and Felderman (1966) and Stanton number, St values (shown below in Eqs. 4, 5)
- Time averaging (mean value integral) is done on the time series to find averaged values over 0.6–1.6 s (where p_0 changes are minimum).

$$q(t) = 2\sqrt{\frac{\rho c k}{\pi}} \sum_{i}^{n} \frac{T_{w(i)} - T_{w(i-1)}}{\sqrt{t_n - t_i} + \sqrt{t_n - t_{i-1}}} \tag{4}$$

where $\rho_{\mathrm{PEEK}} = 1{,}310\,\mathrm{kg/m^3}$, $c_{\mathrm{PEEK}} = 2{,}160$ J/kg K and $k_{\mathrm{PEEK}} = 0.25$ W/m K

$$St(t) = \frac{q(t)}{\rho_\infty u_\infty c_p (T_{\mathrm{aw}} - T_{\mathrm{w}}(t))} \tag{5}$$

where adiabatic wall temperature, T_{aw} is equal to $T_\infty(1 + r\ ((\gamma - 1)/2)\ M_\infty^2)$ and $r = \sqrt{Pr_\infty}$, which is deduced from the free stream conditions for each test.

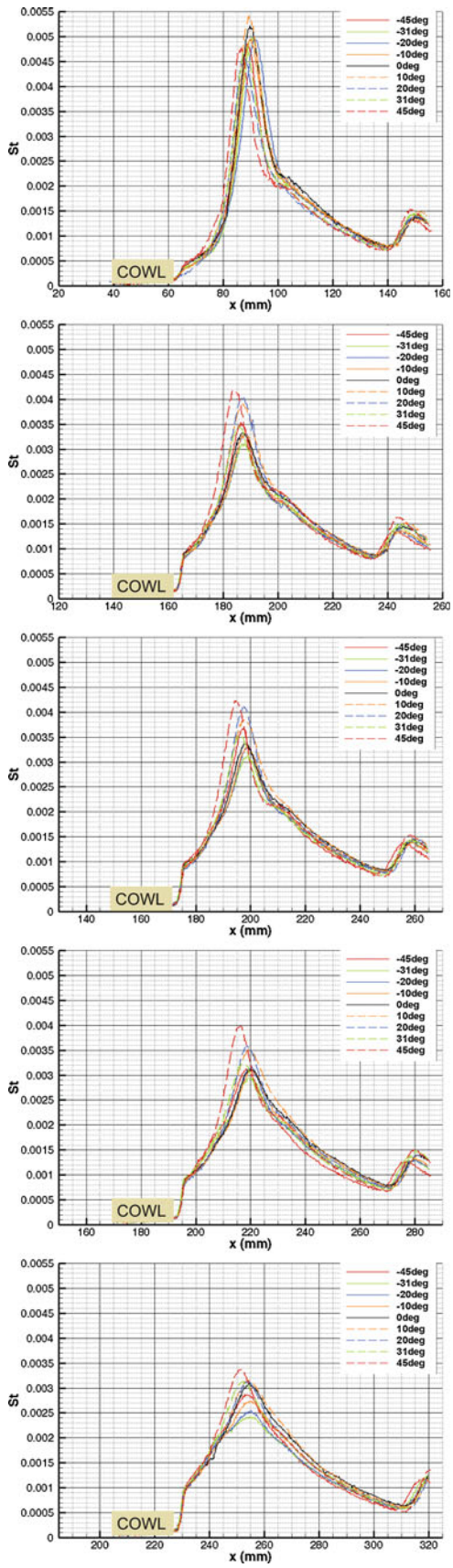

◀ **Fig. 15** Azimuthal distributions of Stanton number for SWBLI@90, 190, 200, 220 and 255 mm cases in descending order

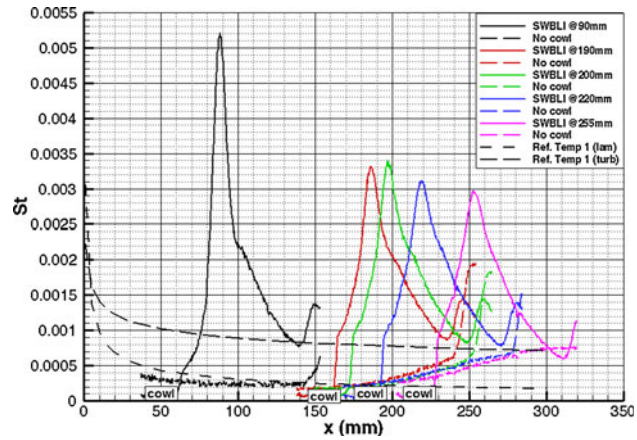

Fig. 16 Centreline Stanton number distributions for all cases with theoretical laminar and turbulent estimates

Table 4 Intermittency values for all cases

Cases	$\varphi(x)$
SWBLI@90 mm	0
SWBLI@190 mm	0.03
SWBLI@200 mm	0.10
SWBLI@220 mm	0.33
SWBLI@255 mm	0.75

It has to be noted that in the current experimental campaign, the initial wall temperature is about 40° K colder than the adiabatic wall temperature, which is around 335 K based on the free stream flow conditions specified in Table 2. Due to the heat transfer from the flow to the surface during the experiments, the centrebody heats up during the tests and the heat transfer reduces. Therefore, time-averaging takes this point into account. In terms of azimuthal data extraction, constant R lines at constant axial location are extracted over the centrebody as shown in Fig. 14 and a correction for the azimuthal angles is conducted using the markers located at −45° and 45°.

Figure 15 shows time-averaged azimuthal Stanton number profiles over the centrebody for all cases. x axis starts from the leading edge of the centrebody. In terms of heat flux peak, the biggest peak is found to be for the nominally laminar case. In this case, the incoming boundary layer is laminar but transition occurs in the separation region which leads to a more important heat flux rise at reattachment much higher than that of a fully laminar interaction. The smallest peak is found to be for the case with highest intermittency, i.e. SWBLI@255 mm

case. For the ones with natural transition, the heat flux peak is highest for SWBLI@200 mm case.

Figure 16 shows Stanton number profiles over the centreline of the centrebody for all the cases. For each case, i.e. SWBLI@90, 190, 200, 220 and 255 mm, the data from the tests without the cowl are also plotted. In addition, theoretical laminar and turbulent distributions of heat flux and Stanton number over a flat plate using reference temperature method (Eckert 1955) are included. The agreement between the experiments and the theory is good in terms of laminar and turbulent heat flux distributions. The transition region is found to be broad, starting from around 150 mm and ending nearly at 300 mm. To find the approximate time-averaged intermittency values, the intermittency function, φ is defined as a function of streamwise coordinate, x, as in Eq. 6.

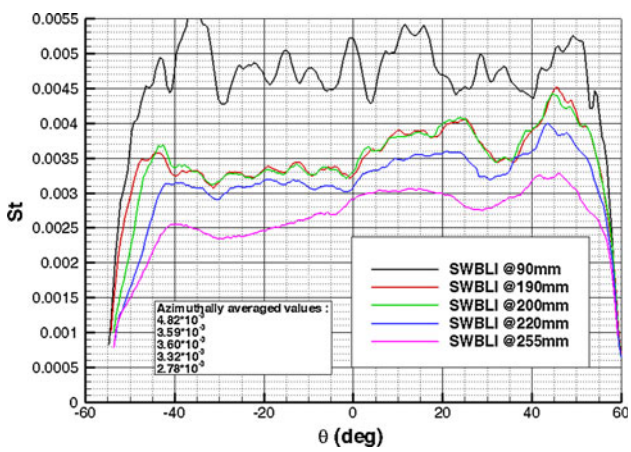

Fig. 17 Azimuthal Stanton number distributions at maximum heat flux lines for all cases

$$\varphi(x) = \frac{St(x) - St_{\text{lam}}(x)}{St_{\text{turb}}(x) - St_{\text{lam}}(x)} \tag{6}$$

where $St_{\text{lam}}(x)$ and $St_{\text{turb}}(x)$ are laminar and turbulent Stanton numbers at a specific streamwise location without SWBLI. On the other hand, $St(x)$ comes from experiments without SWBLI. The intermittency values are tabulated in Table 4.

Figure 17 shows azimuthal Stanton number distributions on max heat flux lines. SWBLI@90 mm shows oscillatory behaviour around the circumference, the reason for that might be the presence of Goertler type vortices. SWBLI@190 and 200 mm cases also exhibit oscillatory behaviour but smaller in peaks and troughs. Another source might be the imperfections on the leading edge inducing well-known streamwise perturbations, which become more evident after SWBLI amplification. SWBLI@200 mm case is very similar to SWBLI@190 mm case in terms of heat flux distribution. Negative azimuthal angles of the centrebody have smaller heat flux values, which is explained in following Sect. 3.3.1. Figure 18 shows the shifted Stanton number distributions over centreline of the centrebody. The horizontal axis is shifted with respect to SWBLI location, i.e. SWBLI location becomes zero. The heat flux rise due to the SWBLI is overlapping on top of each other for SWBLI@190, 200, 220 and 255 cases up to 15 mm upstream of inviscid SWBLI position, afterwards it starts to deviate. The rise is more aggressive for SWBLI@190 and 200 mm cases compared to SWBLI@220 and 255 mm cases. Downstream of heat transfer peak profiles start to overlap around 20 mm downstream of the origin. Smaller rise in profiles at around 50 mm downstream of origin is due to the influence of the nozzle shock. This overlapping behaviour clearly demonstrates the quality and repeatability of the measurements. SWBLI@90 mm case has a

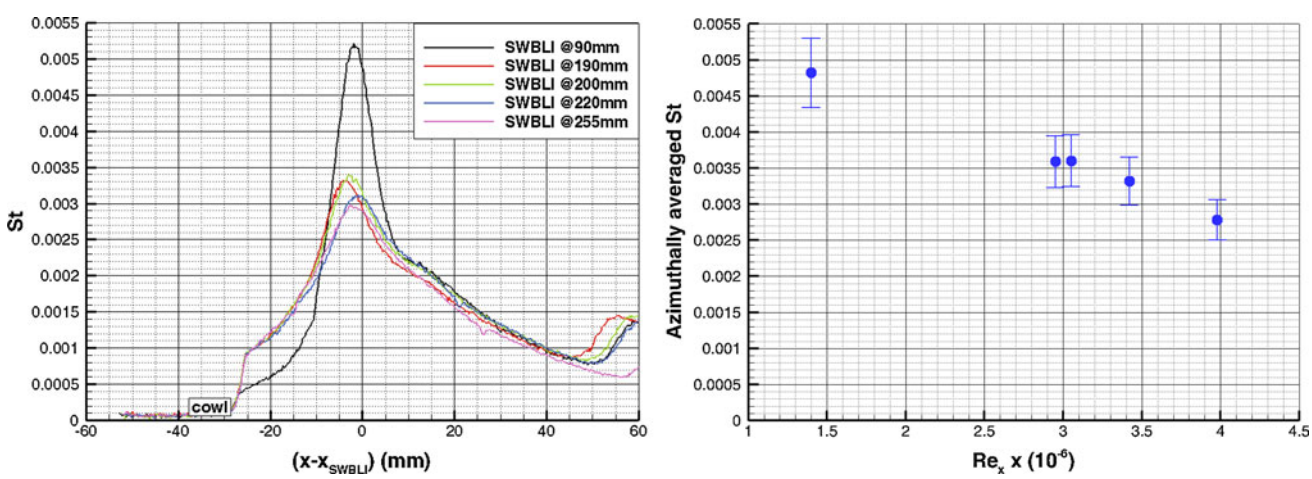

Fig. 18 *Left* centreline Stanton number distributions over the centreline of the centrebody shifted with respect to impinging shock location, *right* azimuthally averaged Stanton number values at maximum q lines versus Reynolds number for all cases

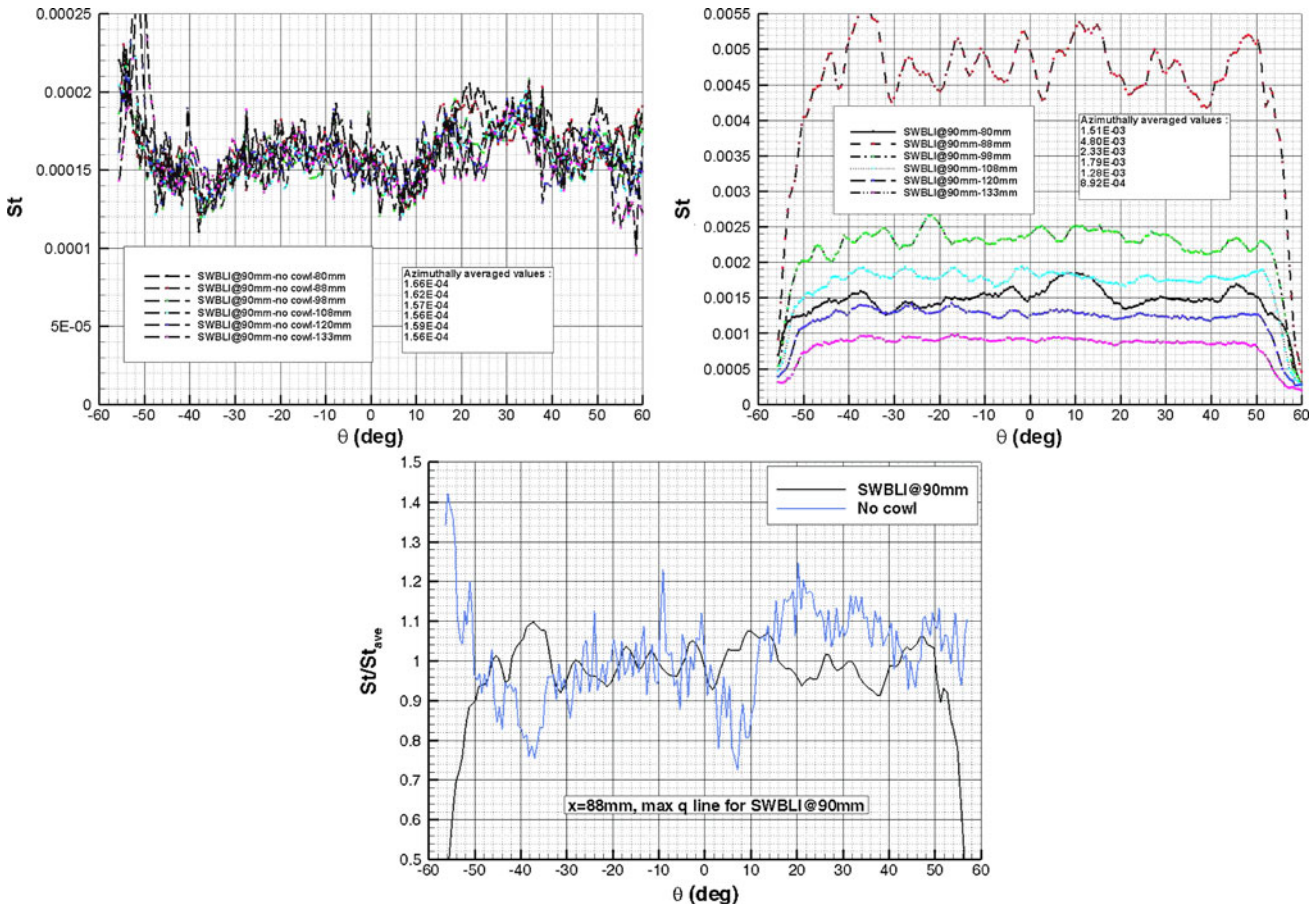

Fig. 19 Azimuthal Stanton number variation along the centrebody, *top left* no cowl, *top right* with 7° cowl, *bottom* comparison at maximum *q* line (i.e. at 88 mm from the leading edge)

bigger heat flux peak and steeper rise due to the fact that the boundary layer is undergoing transition to turbulence (triggered transition) throughout the SWBLI region.

Figure 18 also shows the azimuthally averaged Stanton number values (between −45° and 45° azimuthal angles) at maximum heat flux lines against Reynolds number based on inviscid position of the impinging shock. The error bars do not represent the experimental uncertainties but manifest the variation of heat flux across the circumference between −45° and 45° (from min to max). Nominally, laminar values are found to be biggest, and the highest intermittency values are the smallest. This finding is consistent with the findings from Bur and Chanetz (2009). The uncertainties in the heat flux distributions are found to be around 9 %.

3.3.1 Leading edge effect

The orderly distributed striations observed clearly in SWBLI@90 mm case can stem from leading edge non-uniformities as well as from Goertler type vortices. To critically assess the cause of striations, leading edge thickness measurements are carried out and reported in Sect. 2.3.7. Figure 10 in Sect. 2.3.7 indicates that the section of centrebody with negative azimuthal angles is found to be blunter compared to positive section. As shown in Fig. 19 for SWBLI@90 mm case without and with 7° cowl, Stanton number is relatively smaller on the negative azimuthal angles of the centrebody, especially in between −35° and 5°. This behaviour confirms the hypothesis that transition onset is delayed with bluntness provided that bluntness is not substantial (viscous-dominated transition). Along the centrebody, this azimuthal variation of heat flux prevails, clearly indicating a leading edge effect. With SWBLI, this pattern becomes somewhat orderly distributed in the vicinity of shock impingement location; however, peaks and troughs damp out and profiles become even azimuthally along the centrebody. The bottom plot shows azimuthal Stanton number variation normalised by azimuthally averaged value at the maximum heat flux location on the centrebody for SWBLI@90 mm case without and with impinging shock wave. The disorganised behaviour of without SWBLI case transforms into an ordered pattern. The reason for that

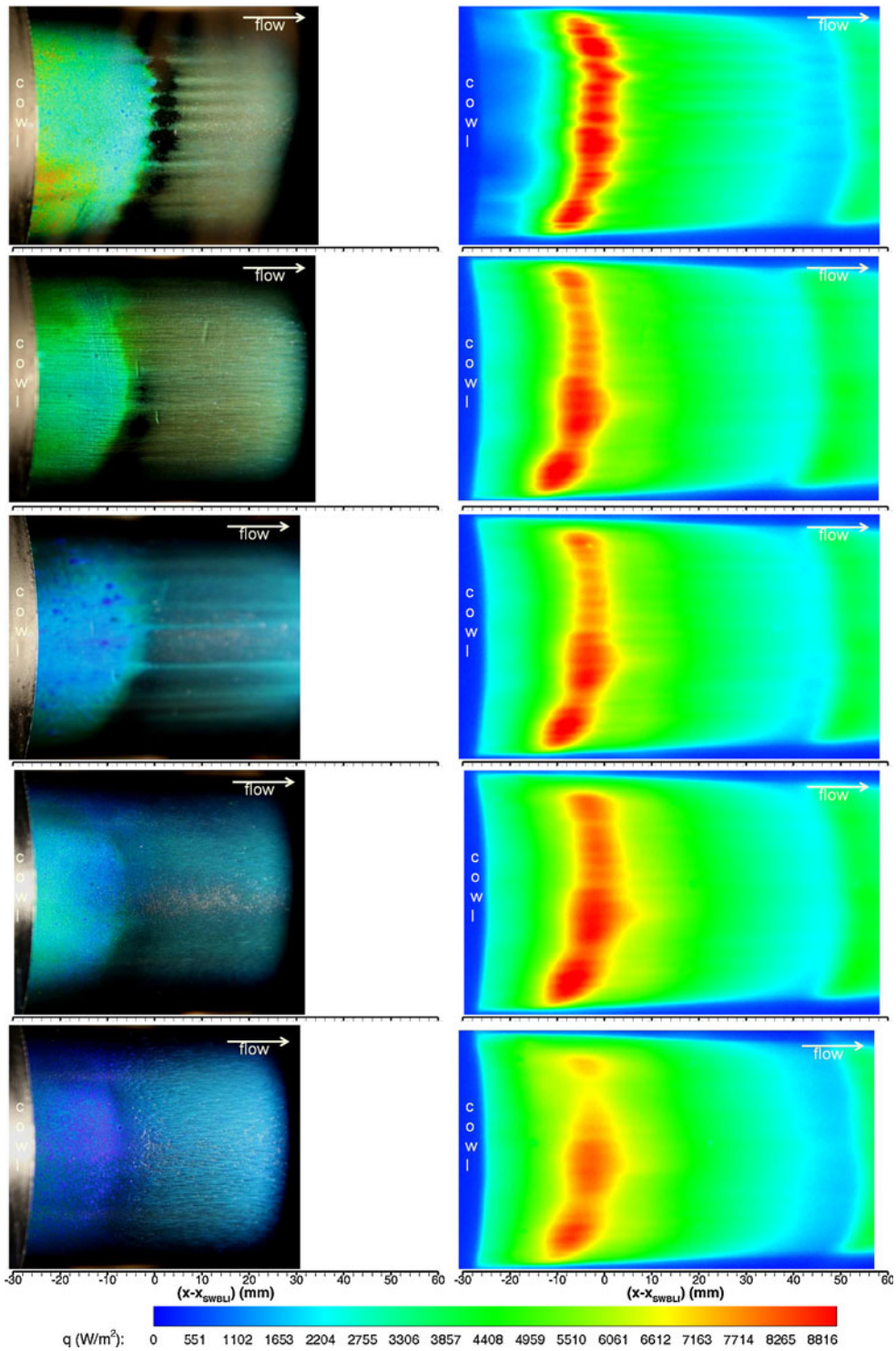

Fig. 20 Liquid crystal visualisation (*left*) and heat flux contours for SWBLI@90, 190, 200, 220 and 255 mm cases in descending order

could be Goertler type vortices, though certain patterns such as peaks and troughs with and without the impinging shock are quite similar. This could also indicate the existence of streamwise perturbations prior to the location of the shock impingement. Therefore, they are referred to as streamwise vortices from this point onwards.

3.4 LC results

Liquid crystals provide qualitative information about wall shear stress field, especially around the reattachment region; the crystal mixture is swept downstream leaving mark on the surface in addition to changing its colour.

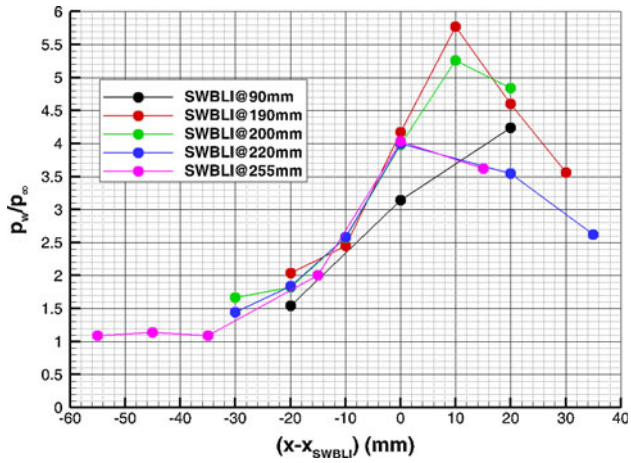

Fig. 21 Nondimensional wall pressure distribution over the centrebody for all cases

Figure 20 shows shear sensitive liquid crystal picture on the left and heat flux contours on the right for all cases. The liquid crystal patterns closely resemble to heat flux contours as expected. It has to be noted that the scale for heat flux contours is set to 9,000 W/m^2 in order to observe SWBLI region clearly. The presence of streamwise vortices is apparent for SWBLI@90 mm case. The leading edge variations are believed to cause streaks through SWBLI region both for SWBLI@190 and 200 mm.

3.5 Wall pressure measurements

In terms of nondimensional wall pressure values, the data reduction procedure is as follows:

- $p_\infty(t)$ is calculated using isentropic relations from measured $p_0(t)$ signal, i.e. $(=p_0(t)/(1+((\gamma-1)/2)M_\infty^2)^{(\gamma-1)/\gamma})$.
- The divided signals of $p(t)/p_\infty(t)$ are obtained.
- These signals are integrated and averaged over time-averaging window between 0.6 and 1.6 s using Eq. 7.

$$\overline{p/p_\infty} = \frac{1}{t_f - t_i}\int_{t_i}^{t_f} p(t)/p_\infty(t)\mathrm{d}t \tag{7}$$

Figure 21 shows shifted nondimensional wall pressure distributions over the centrebody. The horizontal axis is shifted with respect to inviscid SWBLI location, i.e. SWBLI location becomes zero. The pressure rise due to the SWBLI is overlapping on top of each other for SWBLI@190, 200, 220 and 255 mm cases. SWBLI@90 mm case has a steeper rise on the other hand. However, due to the discrete nature of the tappings, the peak of the pressure rise for SWBLI@90 mm case cannot be observed. The maximum nondimensional pressure value is found to be around 5.8. This value is found to be greater than the value of 4.55 found using double regular reflection of 7°. The pattern for the rise of pressure around the SWBLI region is similar for cases with intermittencies, which is more clearly presented in Sect. 3.6. The nondimensional pressure values are found to be accurate within 4 % using an approach from Moffat (1988).

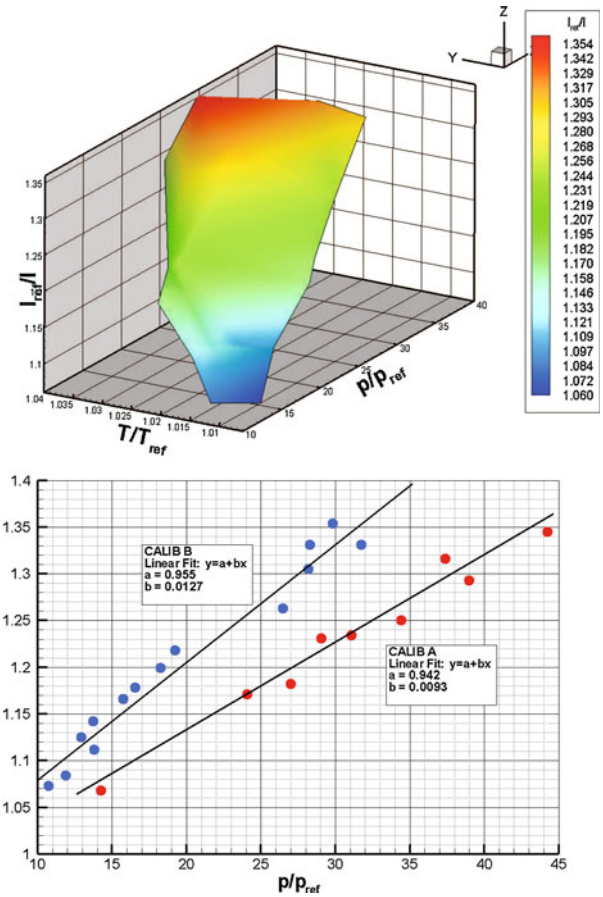

Fig. 22 *Top* in situ calibration map, *bottom*: reduced calibration curves for PSP, i.e. Calib. *A* and *B*

3.6 PSP results

The PSP image acquisition starts before the test run and records for the entire test duration with a frame rate of 9 fps with 8 ms exposure time. A total of 10 images are chosen within the time-averaging window right after stable flow establishment and then averaged for data processing. The reference image is recorded immediately before the test when the model is at vacuum conditions in both pressure and temperature. Dark images are also recorded which is then subtracted from the test and reference images for correction. Afterwards, an intensity ratio image is obtained by dividing the reference image by the correlated test image. Eventually, the intensity ratio is converted to

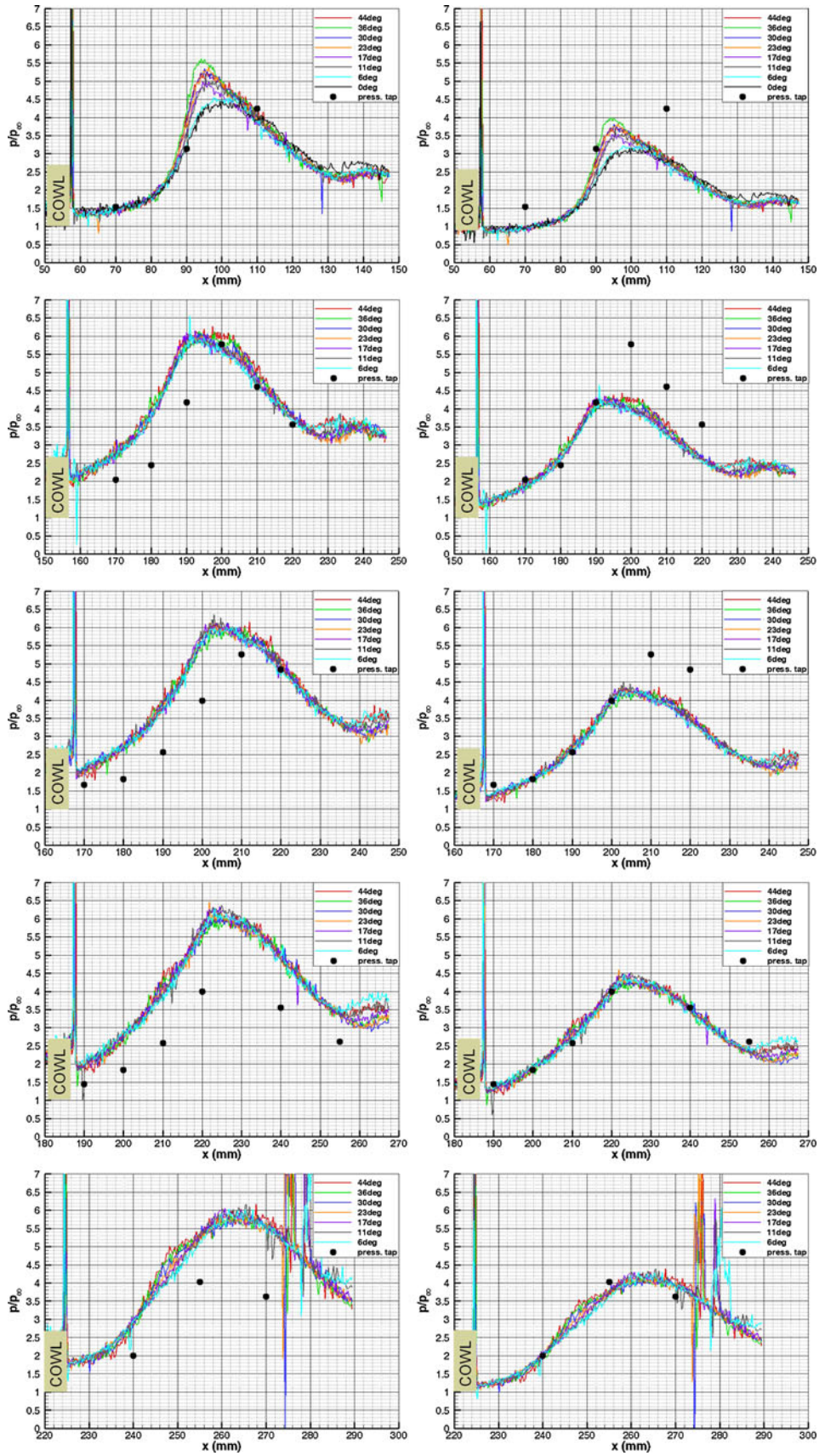

Fig. 23 Nondimensional wall pressure distribution over the centrebody for SWBLI@90, 190, 200, 220 and 255 mm cases in descending order with Calib. *A* (*left*) and Calib. *B* (*right*). Pressure tap data are denoted as *full circles*

pressure distribution using an in situ calibration curve in the form of Eq. 8. In situ calibration implies that p/p_{ref} values are deduced from pressure tapping readings.

$$\frac{I_{ref}}{I} = A(T) + B(T)\left(\frac{p}{p_{ref}}\right)^n \quad (8)$$

The constants A and B are functions of temperature. Figure 22 shows the calibration map (on the top) signifying temperature dependence, a common issue in PSP. However, for a certain value of T/T_{ref} (deduced from QIRT measurements, averaged over time-averaging window) and I_{ref}/I (measured from PSP), a complicated procedure needs to be applied to convert intensity values to pressure values pixel by pixel for each case. In the current tests, a simpler approach is implemented, namely data segmentation. For the upstream regions of SWBLI, a separate calibration is employed, Calib. *B*. Elsewhere, another calibration is employed, Calib. *A*. Linear fits are obtained. These calibrations unfortunately do not overlap at any point of I_{ref}/I for the region of interest as shown in Fig. 22 on the bottom. Therefore, for all the tests, two calibrations are applied.

Figure 23 shows the nondimensional wall pressure distribution over the centrebody with pressure tap data for all tests at various azimuthal locations. Both calibrations are shown for all cases. As the centrebody is rotated 90° for PSP testing (see Fig. 7), the section of the centrebody with negative azimuthal angles is influenced by the local flow going around the cowl stand resulting uneven downstream pressure distributions. Therefore, only positive angles are shown for azimuthal variation. The cowl position manifests itself by a sudden rise and a fall in PSP signal similar to signals around tappings (not shown), and thus, these areas are disregarded. The SWBLI pressure rise is apparent in all cases; the magnitude is the biggest for SWBLI@90 mm laminar case and smallest for SWBLI@255 mm case with highest intermittency similar to findings from QIRT results (see Sect. 3.3). The slope of the rise is increasing until the region close to the peak, which is typical for transitional interactions. Significant variation of peak pressure in azimuthal direction for SWBLI@90 mm case might be explained by the presence of streamwise vortices. The rise broadens with increasing intermittency. The magnitude of the pressure rise is about six times the free stream pressure for SWBLI@190 and 200 mm cases. Generally, the agreement of PSP with tapping data is very good naturally as tap data anchors the PSP response. The values are found to be accurate within 10 % using an approach from Moffat (1988). This estimation omits the substantial discrepancies between the pressure taps and PSP. For instance, if PSP data are based on Calib. *A* and only some of the tappings are used for this calibration, then there is a significant difference between PSP data and the tappings used for Calib. *B*, like in the case of SWBLI@190 mm. Finally, the reason for the significant downstream fluctuations behind the SWBLI region for SWBLI@255 mm case is due to paint removal.

Figure 24 shows simplified behaviour of nondimensional wall pressure distributions over the centrebody. The horizontal axis is shifted with respect to SWBLI location, i.e. SWBLI location becomes zero. For SWBLI@90 mm case, Calib. A is used whereas for SWBLI@220 and 255 mm cases Calib. *B* is utilised with filtering. For the remaining cases, the combination of two PSP calibrations is constructed, where some part of a PSP curve with certain calibration is appended to another PSP curve with different calibration at the other part. The pressure rise due to the SWBLI is overlapping on top of each other for SWBLI@190, 200 and 220 mm cases. SWBLI@90 mm case has an abrupt rise, whereas SWBLI@255 mm case has a gradual behaviour. The locations for the pressure peaks are found to lie between 3 and 8 mm downstream of the inviscid position of the impinging shock. The most downstream position of the pressure peak is observed for SWBLI@255 mm case.

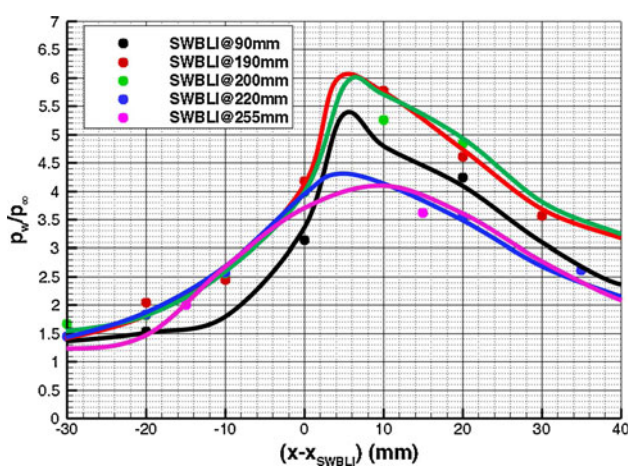

Fig. 24 Simplified behaviour of nondimensional wall pressure distribution over the centrebody for all cases

Table 5 Experimental peak heat flux and peak pressure values with empirical peak heat flux values normalised by reference values

Cases	q_{peak}/q_{ref} exp.	q_{peak}/q_{ref} lam. correl.	q_{peak}/q_{ref} turb. correl.	p_{peak}/p_{ref} exp.
SWBLI@90 mm	12.5	6	3.36	5.4
SWBLI@190 mm	8.1	6	3.36	6.1
SWBLI@200 mm	8.4	6	3.36	6.1
SWBLI@220 mm	6.5	6	3.36	4.3
SWBLI@255 mm	4.6	6	3.36	4.1

The ratios of the peak heat flux and peak pressure to the reference value in the absence of interaction at the same location are tabulated in Table 5 together with empirical laminar and turbulent correlations from Hung and Barnett (1973). In these correlations, nondimensionalised peak heat transfer is expressed as a function of the total inviscid pressure ratio throughout the interaction. In the current case, inviscid pressure ratio of 4.55 is calculated assuming double regular reflection of 7°. Generally, experimental values are found to be higher than the empirical values. Only SWBLI@255 mm case results in a value in between laminar and turbulent empirical values in terms of heat flux. High heat flux peak does not necessarily imply high pressure peak as shown from SWBLI@90 mm case.

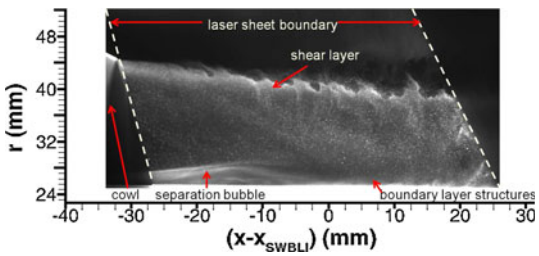

Fig. 25 Raw PIV image showing the flow structures for SWBLI@90 mm case

3.7 PIV results

Two component PIV measurements are done at centreline for SWBLI@90 mm case only. It has to be noted that 3-D flow structures such as streamwise vortices after reattachment cannot be resolved with two-dimensional measurements. The FoV is focussed on interaction region and has the size of 60 × 45 mm^2. Pulse separation between laser pulses, Δt, is set to 0.35 μs so that sufficient displacement for the tracer particles of between 2.3 and 9 pixels for the velocity range from 200 to 800 m/s is ensured. A data set of around 65 instantaneous vector fields is acquired at 15 Hz for three times. Recorded images are divided into initial interrogation windows and then processed with a cross correlation algorithm using DaVis 7.2 software. The initial interrogation area (IA) is selected as 32 × 32 pixel^2 with 2 passes and then refined to 16 × 16 pixel^2 with 3 passes. A 75 % overlap is employed in order to improve spatial resolution and to prevent the appearance of spurious vectors. The signal to noise ratio (SNR, the ratio of the first PIV correlation peak to the second peak) is found to be better than 2.5. The ensemble-averaged results are deduced from the appended data set of 188 vector fields from three repeats for better statistical convergence.

Figure 25 shows the raw PIV image for SWBLI@90 mm case; separation bubble in SWBLI region and downstream boundary layer structures as well as the shear layer at the

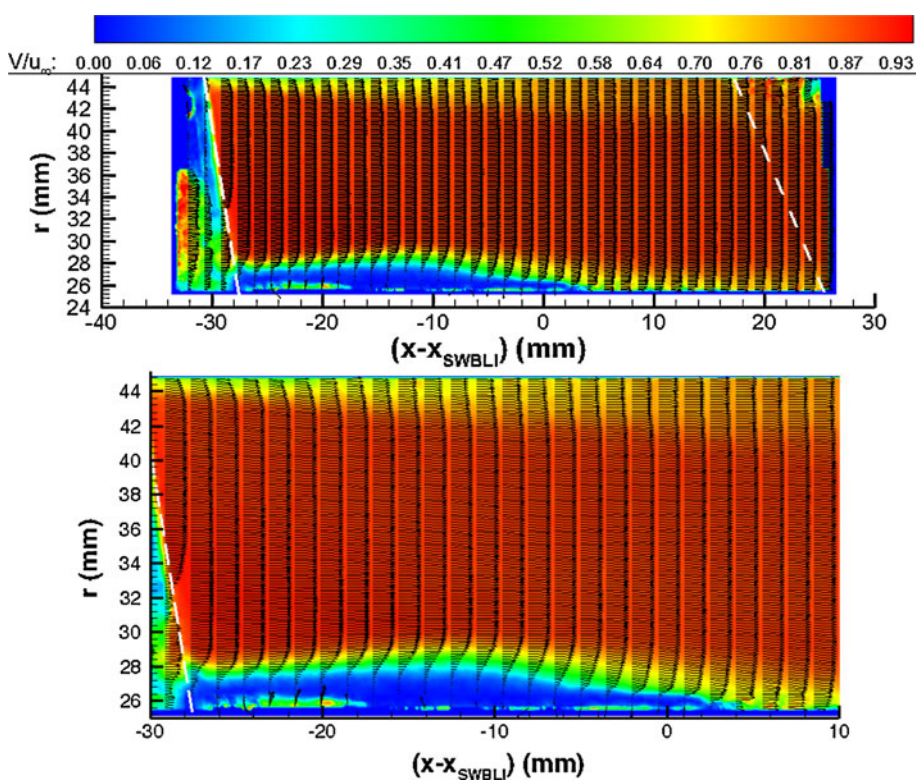

Fig. 26 *Top* ensemble-averaged velocity magnitude contours (m/s) with velocity vectors, *bottom* focussed on SWBLI region

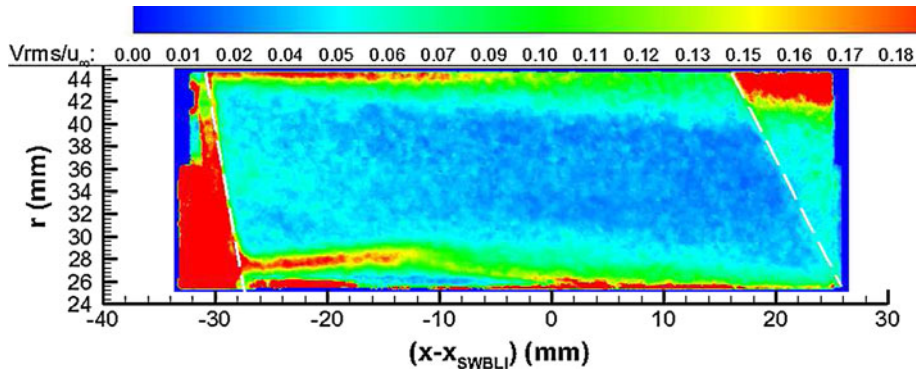

Fig. 27 Ensemble-averaged RMS velocity magnitude contours (m/s)

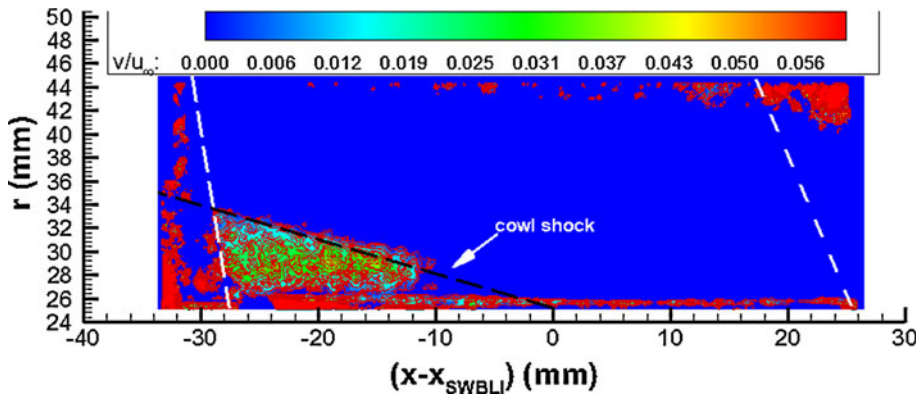

Fig. 28 Ensemble-averaged vertical velocity contours clipped to 0–50 m/s range for SWBLI@90 mm case

cowl trailing edge are apparent. White dashed lines represent the boundaries of the light sheet.

Figure 26 shows ensemble-averaged flow fields in terms of velocity magnitude contours nondimensionalised with free stream velocity. Velocity vectors are also visualised. White lines represent the boundaries of the light sheet; therefore, the vectors outside these boundaries should not be considered. SWBLI region is quite clearly manifested in the bottom plot. The outer flow above the SWBLI region turns towards the wall and becomes parallel after the reattachment. SWBLI has the height of nearly 4 mm and extends about 18 mm downstream of the inviscid position of the impinging shock. In terms of root mean square (RMS) of the velocity fluctuations (see Fig. 27), higher values are obtained at the edge of SWBLI region in vertical direction between 28 and 12 mm upstream of the origin (the possibility of transition mechanism) as well as at the shear layer forming after the cowl trailing edge. The uncertainty in the ensemble-averaged velocities is found be about ±2.4 %, using an approach from Humble (2008).

Figure 28 shows the nondimensionalised (with free stream velocity) vertical velocity contours clipped to 0–0.06 range. The green-coloured patch above the upstream part of the SWBLI region shows the fact that the flow is diverted in vertical direction already before impingement of the shock. This is due to the presence of the separation shock that is visible in Fig. 13. The same area is blurred at the location towards the origin, and this is believed to occur due to the intersection of the separation shock with the impinging shock as well as the particle relaxation distance. Black dashed line represents the inviscid location of the impinging cowl shock.

4 Conclusions

An extensive experimental campaign was carried out to investigate transitional shock wave–boundary layer Interactions at Mach 5 and *Re*/*m* of 15.9×10^6 1/m. An axisymmetric impinging shock that generates 7° flow deflection resulted in separated SWBLI flowfield on axisymmetric centrebody. Various flow diagnostics were utilised to map the complex flowfield such as schlieren photography, QIRT, LC, PSP and pressure tappings and PIV. Centrebody is traversed upstream to localise SWBLI region at various locations/intermittencies. A nominally laminar (triggered transition) case (SWBLI@90 mm) and four natural transition cases with varying intermittency (SWBLI@190, 200, 220 and 255 mm) were tested.

Time-averaged heat transfer and shear stress peaks were found to occur around the reattachment point. For SWBLI@90 mm case, the separation induces transition and the heat transfer was found to be the highest. For the cases with natural transition with different intermittency

levels, where incoming boundary layer is in state of transition, the magnitude of peaks initially started to increase from SWBLI@190 mm case reaching a maximum for SWBLI@200 mm case. Afterwards, the peaks started decreasing towards the highest intermittency case, i.e. SWBLI@255 mm. In terms of pressure peaks, the highest value is found for SWBLI@190 and 200 mm cases.

The influence of leading edge nonuniformities played a significant role in the centrebody only tests which resulted in uneven variation of heat transfer; however, the impinging shock wave made the interaction region azimuthally even. The presence of streamwise vortices was clearly apparent for SWBLI@90 mm case. For SWBLI@190 and 200 mm cases, the leading edge nonuniformities also induced striations yet not in an orderly fashion. LC results showed high levels of wall shear inside the separation region, downstream of the impinging shock position, concurring with QIRT results. Nondimensional pressure peaks, nevertheless, were found to occur slightly upstream of the maximum location of heat flux/shear stress. On the other hand, PIV results (only for SWBLI@90 mm case) showed high levels of turbulence above the separation region, proving triggered transition behaviour.

Acknowledgments The test models were designed by Dr. Nalleli Gongora-Orozco; her and Mr. Mark Quinn's help during the test campaign is greatly acknowledged. The authors would like to thank the technical staff at University of Manchester for their help and assistance. This work has been conducted for European Space Agency (ESA) with a TRP reference number of 2009/666/MPA.

References

Arnal D, Delery J (2004) Laminar–turbulent transition and shock wave/boundary layer interaction. EN-AVT-116-04

Boyce RR, Hillier R (2000) Shock-induced three-dimensional separation of an axisymmetric hypersonic turbulent boundary layer. AIAA paper, 2000-2226

Bur R, Chanetz B (2009) Experimental study on the PRE-X vehicle focusing on the transitional shock-wave/boundary–layer interactions. Aerosp Sci Technol 13:393–401

Cook WJ, Felderman EJ (1966) Reduction of data from thin-film heat transfer gages: a concise numerical technique. AIAA J 4(3): 561–562

Delery J, Marvin JG (1986) Shock wave/boundary layer interactions. AGARDograph no. 280

Dolling DS (2001) Fifty years of shock wave/boundary layer interaction research: what next? AIAA J 39(8):1517–1531

Eckert ERG (1955) Engineering relations for friction and heat transfer to surfaces in high velocity flow. J Aeronaut Sci 22:585–587

Edney B (1968) Anomalous heat transfer and pressure distributions on blunt bodies at hypersonic speeds in the presence of an impinging shock. FFA Report 115. Aeronautical Research Institute of Sweden, Stockholm

Erdem E, Kontis K (2010) Numerical and experimental investigation of transverse injection flows. J Shock Waves 20(2):103–118

Erdem E, Saravanan S, Lin J, Kontis K (2012a) Experimental investigation of transverse injection flowfield at mach 5 and the influence of impinging shock wave. In: 18th AIAA/3AF international space planes and hypersonic systems and technologies conference, Tours, France

Erdem E, Saravanan S, Kontis K (2012b) Air, carbon dioxide and helium transverse sonic jets in Mach 5 cross flow. In: 9th international ERCOFTAC symposium on engineering turbulence modeling and measurements, Thessaloniki, Greece

Erdem E, Yang L, Kontis K (2012c) Steady energy deposition at Mach 5 for drag reduction. J. Shock Waves 20(2):103–118

Holden M (1986) A review of aerothermal problems associated with hypersonic flights. AIAA Paper 77-0045

Humble RA (2008) Unsteady flow organization of a shock wave boundary layer interaction. PhD thesis, Delft University of Technology

Humble RA, Scarano F, van Oudheusden BW (2007) Particle image velocimetry measurements of a shock wave/turbulent boundary layer interaction. Exp Fluids 43:173–183

Humble RA, Scarano F, van Oudheusden BW (2009) Unsteady aspects of an incident shock wave/turbulent boundary layer interaction. J Fluid Mech 635:47–74

Hung FT, Barnett DO (1973) Shock wave/boundary layer interference heating analysis. AIAA Paper 72-0237

Knight D, Yana H, Panaras AG, Zheltovodov A (2003) Advances in CFD prediction of shockwave turbulent boundary layer interactions. Prog Aerosp Sci 39:121–184

Kontis K, Stollery JL (1999) Incipient separation on flared bodies at hypersonic speeds. Aeronaut J 103(1027):405–414

Melling A (1997) Tracer particles and seeding for particle image velocimetry. Meas Sci Technol 8:1406–1416

Moffat RJ (1988) Describing the uncertainties in experimental results. Exp Therm Fluid Sci 1(1):3–17

Murray N, Hillier R, Williams S (2013) Experimental investigation of axisymmetric hypersonic shock-wave/turbulent-boundary–layer interactions. J. Fluid Mech 714:152–189

Quinn MK, Yang L, Kontis K (2011) Pressure-sensitive paint: effect of substrate. Sensors 11:11649–11663

Samimy M, Lele SK (1991) Motion of particles with inertia in a compressible free shear layer. Phys Fluids A 3:1915–1923

Scarano F (2008) Overview of PIV in supersonic flows. In: Schroeder A, Willert CE (eds) Particle Image Velocimetry, Topics in Applied Physics, vol 112, pp 445–463

Schuelein E, Krogmann P, Stanewsky E (1996) Documentation of two-dimensional impinging shock/turbulent boundary layer interaction flow. DLR/IB 223-96 A 49

Settles GS (1993) Swept shock/boundary layer interaction scaling laws, flow field structure and experimental methods. AGARD/FDP VKI special course on shock wave/boundary layer interactions in supersonic and hypersonic flows. AGARD Report No. 792

Settles GS, Dodson LJ (1991) Hypersonic shock/boundary layer database. NASA CR 177577

Simeonides GA (2003) Correlation of laminar-turbulent transition data over flat plates in supersonic/hypersonic flow including leading edge bluntness effects. J Shock Waves 12:497–508

Steelant J (2002) Effect of a compressibility correction on different turbulence models. In: 5th international ERCOFTAC symposium on engineering turbulence modeling and measurements, Mallorca, Spain

Steelant J, Dick E (2001) Modeling of laminar–turbulent transition for high freestream turbulence. J Fluids Eng 123(1):22–30

Vandomme L, Chanetz B, Benay R, Perraud J (2006) Shockwave/transitional boundary-layer interactions in hypersonic flow. AIAA J 44(6):1243–1254

Yang L, Zare-Behtash H, Erdem E, Kontis K (2011) Application of AA-PSP to hypersonic flows: the double ramp model. Sens Actuators B 161:100–107

Yang L, Erdem E, Zare-Behtash H, Kontis K, Saravanan S (2012a) Pressure-sensitive paint on a truncated cone in hypersonic flow at incidences. Int J Heat Fluid Flow 37:9–21

Yang L, Zare-Behtash H, Erdem E, Kontis K (2012b) Investigation of the double ramp in hypersonic flow using luminescent measurement systems. Exp Therm Fluid Sci 40:50–56